

# Distributed quantum sensing in a continuous variable entangled network

Xueshi Guo,<sup>1,\*</sup> Casper R. Breum,<sup>1</sup> Johannes Borregaard,<sup>2</sup> Shuro Izumi,<sup>1</sup> Mikkel V. Larsen,<sup>1</sup> Matthias Christandl,<sup>2</sup> Jonas S. Neergaard-Nielsen,<sup>1,†</sup> Ulrik L. Andersen<sup>1,‡</sup>

<sup>1</sup>*Center for Macroscopic Quantum States (bigQ), Department of Physics, Technical University of Denmark, Fysikvej, 2800 Kgs. Lyngby, Denmark*

<sup>2</sup>*QMATH, Department of Mathematical Sciences, University of Copenhagen, Universitetsparken 5, 2100 Copenhagen, Denmark*  
(Dated: June 9, 2022)

Networking plays a ubiquitous role in quantum technology [1, 2]. It is an integral part of quantum communication and has significant potential for upscaling quantum computer technologies that are otherwise not scalable [3]. Recently, it was realized that sensing of multiple spatially distributed parameters may also benefit from an entangled quantum network [4–9]. Here we experimentally demonstrate how sensing of an averaged phase shift among four distributed nodes benefits from an entangled quantum network. Using a four-mode entangled continuous variable (CV) state, we demonstrate deterministic quantum phase sensing with a precision beyond what is attainable with separable probes. The techniques behind this result can have direct applications in a number of primitives ranging from biological imaging to quantum networks of atomic clocks.

Quantum noise associated with quantum states of light and matter ultimately limits the precision by which measurements can be carried out [10–12]. However, by carefully designing the coherence of this quantum noise to exhibit properties such as entanglement and squeezing, it is possible to measure various physical parameters with significantly improved sensitivity compared to classical sensing schemes. Numerous realizations of quantum sensing utilizing non-classical states of light [2, 13, 15] and matter [16] have been reported, while only a few applications have been explored. Examples are quantum-enhanced gravitational waves interferometry [17], detection of magnetic fields [18–20] and sensing of the viscous-elasticity parameter of yeast cells [21]. All these implementations are, however, restricted to the sensing of a single parameter at a single location.

Spatially distributed sensing of parameters at multiple locations in a network is relevant for applications from local beam tracking [22] to global scale clock synchronization [4]. The development of quantum networks [1, 2, 23, 24] enables new strategies for enhanced performance in such scenarios. Theoretical works [5–8, 25–28] have shown that entanglement can improve sensing capabilities in a network using either twin-photons

or Greenberger-Horne-Zeilinger (GHZ) states combined with photon number resolving detectors [6, 7] or using CV entanglement for the detection of distributed phase space displacements [8]. In this Letter, we experimentally demonstrate an entangled CV network for sensing of multiple phase shifts inspired by the theoretical proposal of Ref. [8]. Moreover, for the first time in any system, we demonstrate deterministic distributed sensing in a network of four nodes with a sensitivity beyond that achievable with a separable approach using similar quantum states.

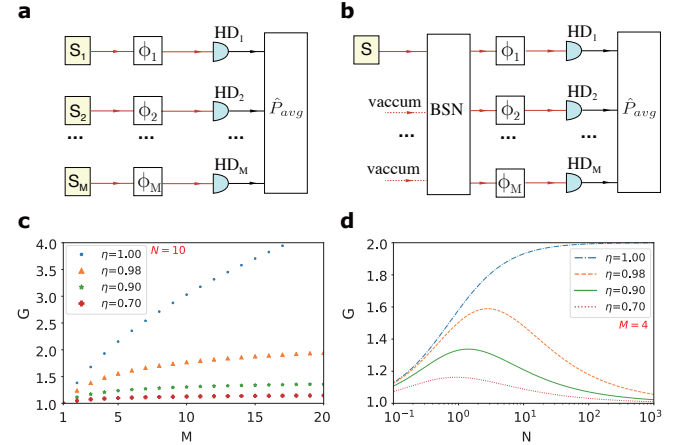


**FIG. 1. Distributed phase sensing scheme.** The task is to estimate the average value of  $M$  spatially distributed phase shifts  $\phi_1, \dots, \phi_M$ . **(a)** Without a network, the average phase shift must be estimated by probing each sample individually. This can be done with homodyne detection of the phase quadrature ( $HD_1, \dots, HD_M$ ), and the sensitivity can be increased by using squeezed probes generated by  $M$  independent squeezers  $S_1, \dots, S_M$ . **(b)** If the  $M$  sites are connected by an optical beam splitter network (BSN), a single squeezed probe can be distributed among the sites. This enables entanglement-enhanced sensing of the average phase shift. **(c,d)** The entangled approach of panel (b) shows a gain in sensitivity compared to the separable approach in panel (a) for the same number of photons,  $N$ , hitting each sample and with optimized probe states. This gain,  $G = \sigma_s^{\text{opt}} / \sigma_e^{\text{opt}}$ , is here plotted as a function of the number of samples  $M$  with  $N$  fixed at 10 (c) and as a function of the average number of photons with  $M$  fixed at 4 (d) for different values of  $\eta$ , the efficiency of the channel between pure resource state and phase sample.

\* E-mail: xguo@fysik.dtu.dk

† E-mail: jsne@fysik.dtu.dk

‡ E-mail: ulrik.andersen@fysik.dtu.dk

We start by introducing a theoretical analysis of the

networked sensing scheme. Consider a network of  $M$  nodes with optical inputs that undergo individual phase shifts,  $\phi_j$  ( $j = 1, \dots, M$ ). The goal is to estimate the averaged phase shift,  $\phi_{\text{avg}} = \sum_{j=1}^M \phi_j / M$ , among all nodes with as high precision as possible. Two different sensing setups are considered: A separable system where the nodes are interrogated with independent quantum states (Figure 1a) and an entangled system where they are interrogated with a joint quantum state (Figure 1b). We assume the optical probes to be arbitrary pure Gaussian quantum states described by the state vectors  $\hat{D}(\alpha)\hat{S}(r)|0\rangle$ , where  $\hat{D}$  and  $\hat{S}$  are the displacement and squeezing operators, respectively,  $\alpha$  is the displacement amplitude and  $r$  is the squeezing factor. We assume that each probe state undergoes loss in a channel with transmission  $\eta$ . We furthermore restrict the estimator to be the joint phase quadrature,  $\hat{P}_{\text{avg}} = \sum_{j=1}^M \hat{p}_j / M$  (where  $\hat{p}_j$  are the phase quadratures of the individual modes), practically corresponding to the averaged outcome of  $M$  individual homodyne detectors. These states and detectors are of particular interest due to their experimental feasibility, inherent deterministic nature, high efficiency, and robustness to noise.

Using the separable approach,  $M$  identical Gaussian probe states are prepared and individually detected, while in the entangled approach, a single squeezed Gaussian state is distributed evenly to the  $M$  nodes via a beam splitter array and likewise measured individually with homodyne detectors at the nodes. If one wanted to estimate different linear combinations of the phase shifts than the simple average, other beam splitter divisions would be required [5, 6]. The sensitivity of the measurement can be defined as the standard deviation of the measurement which, by error propagation, is [12]

$$\sigma = \frac{\sqrt{\langle \Delta \hat{P}_{\text{avg}}^2 \rangle}}{|\partial \langle \hat{P}_{\text{avg}} \rangle / \partial \phi_{\text{avg}}|}, \quad (1)$$

where  $\langle \Delta \hat{P}_{\text{avg}}^2 \rangle = \langle \hat{P}_{\text{avg}}^2 \rangle - \langle \hat{P}_{\text{avg}} \rangle^2$  is the variance of the estimator. We are only interested in the sensitivity for small phase shifts, since one can always use an initial rough phase estimation to adjust the homodyne detector (the local oscillator phase) to the maximum sensitivity setting [2]. For small phase shifts, we obtain the sensitivities for the separable ( $\sigma_s$ ) and entangled ( $\sigma_e$ ) approaches (see Supplementary Material Sec. I):

$$\sigma_s = \frac{\sqrt{e^{-2r_s} + 1/\eta - 1}}{2\alpha_s\sqrt{M}}, \quad (2)$$

$$\sigma_e = \frac{\sqrt{e^{-2r_e} + 1/\eta - 1}}{2\alpha_e}. \quad (3)$$

We now constrain the average number of photons,  $N$ , hitting each sample. The photons can be separated into those originating from coherent displacement and those originating from squeezing:  $N = N_{s,\text{coh}} + N_{s,\text{sqz}} = \eta(\alpha_s^2 + \sinh^2 r_s)$  for the separable case and  $N = N_{e,\text{coh}} +$

$N_{e,\text{sqz}} = \eta(\alpha_e^2 + \sinh^2 r_e)/M$  for the entangled case. The ratio between photon numbers, parametrized as  $\mu_{s(e)} = N_{s(e),\text{sqz}}/N$  can be tuned to give the optimal sensitivities

$$\sigma_s^{\text{opt}} = \frac{1}{2\sqrt{MN}} \sqrt{\frac{N(1-\eta) + \frac{\eta}{2}(1 + \sqrt{1 + 4N(1-\eta)})}{1 + \eta/N}}, \quad (4)$$

$$\sigma_e^{\text{opt}} = \frac{1}{2MN} \sqrt{\frac{MN(1-\eta) + \frac{\eta}{2}(1 + \sqrt{1 + 4MN(1-\eta)})}{1 + \eta/(MN)}}. \quad (5)$$

For perfect efficiency ( $\eta = 1$ ), it is clear that the sensitivity of the entangled system yields Heisenberg scaling both in the number of nodes ( $1/M$ ) and the number of photons per mode ( $1/N$ ) whereas the separable system only achieves the latter and a classical  $1/\sqrt{M}$ -scaling with the number of modes. The gain in sensitivity of the entangled network relative to the separable network (denoted  $G = \sigma_s^{\text{opt}}/\sigma_e^{\text{opt}}$ ) is thus  $G = \sqrt{M}$ .

For non-ideal efficiency, the Heisenberg scaling ceases to exist. In fact, for  $\eta \rightarrow 0$ , both sensitivities approach  $1/2\sqrt{MN}$ . Still, it is important to note that the entangled network exhibits superior behavior for any value of  $\eta$ ,  $M$  and  $N$  for optimized  $\mu$ . Some examples for the sensitivity gain are illustrated in Figures 1c and d. From Fig 1d where a network of  $M = 4$  nodes is considered, it is clear that the highest gain in sensitivity is attained at a finite photon number. We also note that for large photon numbers, the gain tends to unity for non-zero loss meaning no enhanced sensitivity when using the entangled approach. However, there is still a saving in the amount of resources needed to reach the same sensitivity: Only one squeezer is needed compared to the  $M$  squeezers with similar squeezing levels for the separable approach (see Supplementary Material Sec. I).

Next, we demonstrate experimentally the superiority of using an entangled network for distributed sensing. The entangled network is realized by dividing equally a displaced single mode squeezed state into four spatial modes by means of three balanced beam splitters (Fig. 2a, see Supplementary Sec. III for more details). These modes are then sent to the four nodes of the network at which they each undergo a phase shift  $\phi_j$  and are finally measured with high-efficiency homodyne detectors (HD) that are set to measure the phase quadrature,  $\hat{p}_j$ . The resulting photo-currents from the four detectors are further processed and subsequently combined to produce the averaged phase shift. For demonstration purpose, we set all  $\phi_j$  to the same value  $\phi_j = \phi_{\text{avg}}$ , but in principle they could be different.

We prepare the displaced squeezed state by injecting a coherent state into an optical parametric oscillator (OPO) operating below threshold. To avoid low frequency technical noise, the coherent state is produced at a 3 MHz sideband relative to the carrier frequency using an electro-optical phase modulator (EOM) preceding the OPO. The excitation of the coherent state at

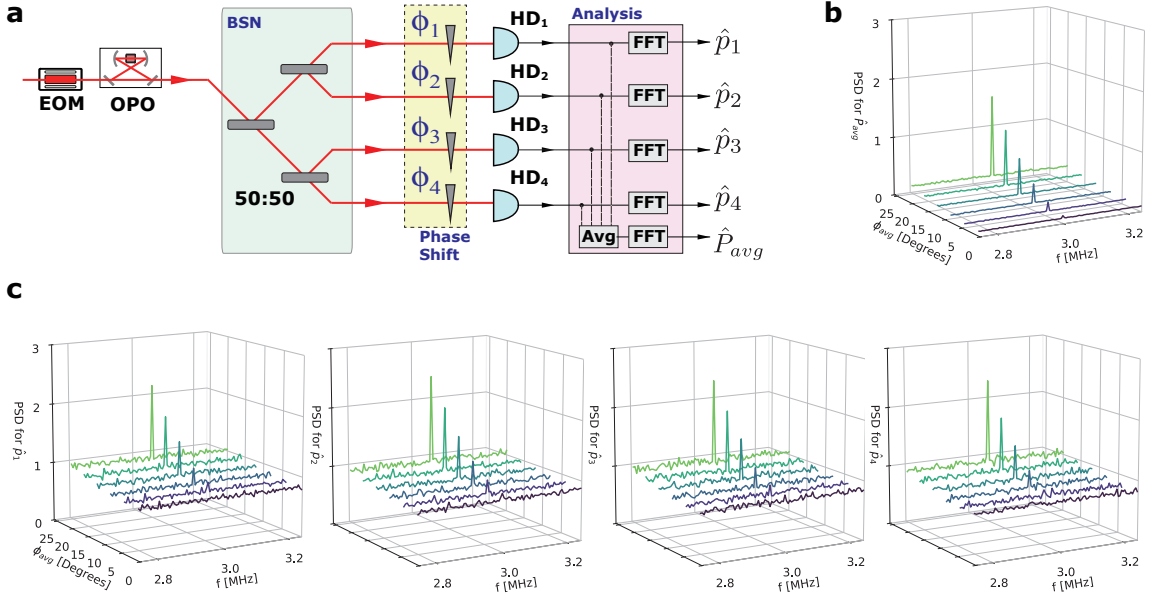


**FIG. 2. Experimental setup and data.** (a) A schematic outline of the experimental setup for the entangled approach with  $M = 4$  (see Supplementary Material Sec. III for more details). A 1550 nm laser beam is phase-modulated at 3 MHz by an electro-optic modulator (EOM) and injected into an optical parametric oscillator (OPO). This prepares a displaced squeezed state at the 3 MHz side-band. A beam-splitter network (BSN) splits the state into four identical and entangled probes which are used to sense the average phase shift of  $\phi_1$  to  $\phi_4$  introduced by four  $\lambda/2$  wave-plates. After phase shifting, the probes' phase quadratures  $\hat{p}_j$  are measured with homodyne detection setups (HD<sub>1</sub> to HD<sub>4</sub>) whose outputs are recorded by an oscilloscope. The power spectral densities (PSD) of the individual modes as well as the average of them,  $\hat{P}_{\text{avg}}$ , are obtained from Fourier transformations (FFT) of the oscilloscope traces. This setup can be reduced to the separable approach ( $M = 1$ ) by removing the BSN and sending the state to one phase shift and HD. (b,c) PSD results for  $\hat{P}_{\text{avg}}$  (b) and  $\hat{p}_j$  (c) from one experimental run for the entangled approach  $M = 4$ . We rotate all the  $\lambda/2$  wave-plates by  $1^\circ$  and measure the side-band spectra for different  $\phi_{\text{avg}}$ , which are known in advance through phase calibration (Supplementary Sec. IV). From these spectra,  $\langle \hat{P}_{\text{avg}} \rangle$  and  $\langle \Delta \hat{P}_{\text{avg}}^2 \rangle$ , which constitute the sensitivity  $\sigma$ , are extracted: The peak and the noise level of the spectrum for  $\hat{P}_{\text{avg}}$  are respectively given by  $\langle \hat{P}_{\text{avg}}^2 \rangle$  and  $\langle \Delta \hat{P}_{\text{avg}}^2 \rangle = \langle \hat{P}_{\text{avg}}^2 \rangle - \langle \hat{P}_{\text{avg}} \rangle^2$ .

3 MHz is thus  $90^\circ$  out of phase with the carrier excitation. The maximum squeezing measured through the joint measurement of 4 HDs is  $\sim 5$  dB at 3 MHz.

An experimental run is shown in Fig. 2b. In this particular run, a displaced squeezed state with an average photon number of  $N = 2.48 \pm 0.12$  in each mode is prepared of which  $N_{e,\text{sqz}} = 0.30 \pm 0.01$  photons are from the squeezing operation and  $N_{e,\text{coh}} = 2.19 \pm 0.11$  are from the EOM as this distribution is near-optimal for the entangled case. We then impose 12 different  $\phi_{\text{avg}}$  values by phase shifts at each node while recording the Fourier transformed homodyne detector outputs; the spectra around the 3 MHz sideband for six of the  $\phi_{\text{avg}}$  values are shown in Fig. 2b (see Supplementary Sec. V for more details). These outputs yield poor estimates of the individual phase shifts (because the squeezing in each mode is only  $\sim 0.8$  dB) but the averaged phase shift obtained by summing the photo-currents produces an entanglement-enhanced estimate with significantly lower noise. The spectra for the averaged photo-currents are shown in Figure 2c. For comparison, we also simulate the separable approach by directing the entire displaced squeezed state (with properly optimized pa-

rameters) to a single node. We then perform the phase estimation at that node and scale the obtained sensitivity by  $\sqrt{4}$  to get the projected performance for an average over four identical sites. An example is shown in Fig 2b for  $N = 2.63 \pm 0.11$ , with  $N_{s,\text{sqz}} = 0.31 \pm 0.01$  and  $N_{s,\text{coh}} = 2.32 \pm 0.10$ .

We quantify the performance of the sensing network by estimating the sensitivities of the two approaches based on the averaged homodyne measurement outcomes,  $P_{\text{avg}}$ . By extracting the rate of change with respect to a phase rotation,  $|\partial \langle \hat{P}_{\text{avg}} \rangle / \partial \phi_{\text{avg}}|$ , as well as the variance,  $\langle \Delta \hat{P}_{\text{avg}}^2 \rangle$ , of  $P_{\text{avg}}$ , we deduce the sensitivity using Eq. (1). For the experimental runs described above, we obtain sensitivities of  $\sigma_e = 0.099 \pm 0.003$  and  $\sigma_s = 0.118 \pm 0.002$  for the entangled and separable approach, respectively. This corresponds to single shot resolvable distributed phase shifts (that is, phase shifts for which the signal-to-noise ratio is unity) of  $5.66^\circ \pm 0.18^\circ$  for the entangled case and  $6.76^\circ \pm 0.11^\circ$  for the separable case with  $\sim 2.5$  photons. Using a coherent state in replacement of the squeezed state, the minimal resolvable phase for 2.5 photons is  $9.06^\circ \pm 0.07^\circ$  corresponding to the standard quantum limit. Note that these angles are larger than our

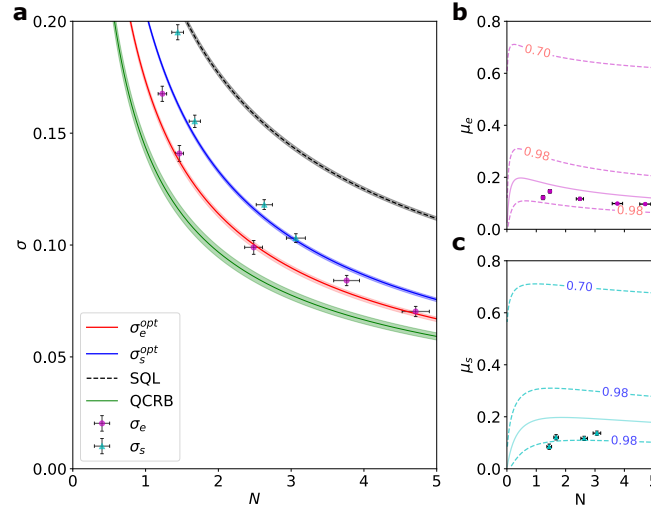


FIG. 3. **Phase sensitivity results.** (a) Sensitivity to  $\phi_{\text{avg}}$  for different average number of photons per sample  $N$  for the entangled scheme ( $\sigma_e$ ) and the separable scheme ( $\sigma_s$ ). The sensitivities predicted in theory,  $\sigma_e^{\text{opt}}/\sigma_s^{\text{opt}}$ , are plotted with shadowed lines, where the shadows show the upper/lower bound within the overall efficiency  $\eta = 73.5\% \pm 1.5\%$  of our experimental setup. SQL: the standard quantum limit, for which no squeezer but only coherent states are used. QCRB: the lower limit of the Quantum Cramér-Rao bound of the entangled approach for our detection efficiency (see Supplemental Material Sec. II for more details). (b) Data points are the values of  $\mu_e$  (the proportion of  $N$  originating from the squeezing process) obtained in the experiment. The solid curves are the optimal  $\mu_e$  that minimize  $\sigma$  at a given  $N$ . The contours indicate the values of  $\sigma_e^{\text{opt}}/\sigma_e$ . (c) As (b), but for the separable approach.

small phase shift approximation (which requires  $\phi_{\text{avg}}$  to be much smaller than  $\sim 7^\circ$  for the conditions in this experimental run, see Supplementary Sec. I). In practice this can be resolved by probing the samples many times ( $K$ ) and get  $\sqrt{K}$  times smaller resolvable phase shift angles.

We find the sensitivities for different total average photon numbers both for the entangled and separable network, and plot the results in Figure 3a. For every selection of the total photon number, we adjust  $\mu$  to a near-optimal value for optimized sensitivity (Figure 3b,c). It is clear in Figure 3a that both realizations beat the standard quantum limit (reachable by coherent states of light), and most importantly, we see that the entangled network outperforms the separable network. The ultimate sensitivity bound of our entangled approach, which is confined by the lower limit of the quantum Cramér Rao bound (shown as QCRB in Figure 3), is not reached in our implementation. However, homodyne detection will not even in principle saturate this bound and non-Gaussian measurements are in general needed (see Supplementary Material Sec. II).

Our results experimentally demonstrate how mode entanglement can enhance the sensitivity in a distributed sensing scenario. Importantly, we show this enhancement in an experimentally feasible setting where the sensitivity of standard coherent probes are enhanced through quadrature squeezing. This approach allows for easy tunable probe powers in order to adapt the setup to the specific application. Consequently, we believe that techniques demonstrated here have direct applications in a

number of areas. Specifically, beam tracking relevant for molecular tracking and biological imaging [21, 22] could directly benefit from these techniques. Such applications impose limits on the allowed probe power to prevent photon damage and heating of the systems. Mode-entanglement can thus be used to increase sensitivity without increasing the probe power. Using squeezed coherent light for quantum non-demolition (QND) measurement has also been exploited for generation of spin squeezing in atomic ensembles [29] and optical magnetometry [18]. While this is usually considered for single ensembles, the generalization to multiple ensembles can provide enhanced sensitivity and new primitives for quantum information processing. Combining several ensembles for magnetometry and utilizing mode-entanglement would further reduce the shot-noise and increase sensitivity of a collective optical measurement. Performing a collective optical QND measurement of several atomic ensembles can prepare a distributed spin-squeezed state for quantum network applications. In particular, squeezing of multiple optical lattice clocks could be used for collective enhancement of clock stability [4, 30]. In Ref. [30], this was obtained by letting a single probe interact with all ensembles in a sequential manner. However, utilizing mode-entanglement, this can be performed in a parallel fashion with no quantum signal being transmitted between the ensembles.

## DATA AVAILABILITY



Experimental data and analysis code is available on request.

## Acknowledgments

M.C. and J.B. acknowledge support from VILLUM FONDEN via the QMATH Centre of Excellence (Grant no. 10059) and the European Research Council (ERC Grant Agreements no 337603). X.G., C.B., S.I., M.L., J.N. and U.A. acknowledge support from Center for Macroscopic Quantum States (bigQ DNR142). X.G., S.I. and J.N. acknowledge support from VILLUM FONDEN via the Young Investigator Programme (Grant

no. 10119).

## AUTHOR CONTRIBUTIONS

J.B., U.A., J.N. and X.G. conceived the experiment. X.G., C.B. and M.L. performed the experiment and analyzed the data. J.B., S.I., J.N., X.G. and M.C. worked on the theoretical analysis. All authors contributed to the manuscript.

## ADDITIONAL INFORMATION

**Competing interests:** The authors declare that there are no competing interests.

- 
- [1] H. J. Kimble, *Nature* **453**, 1023 (2008).
  - [2] S. Wehner, D. Elkouss, and R. Hanson, *Science* **362**, 9288 (2018).
  - [3] N. H. Nickerson, Y. Li, and S. C. Benjamin, *Nature Communications* **4**, 1756 (2013).
  - [4] P. Kómár, E. M. Kessler, M. Bishof, L. Jiang, A. S. Sørensen, J. Ye, and M. D. Lukin, *Nature Physics* **10**, 582 (2014).
  - [5] Z. Eldredge, M. Foss-Feig, J. A. Gross, S. L. Rolston, and A. V. Gorshkov, *Phys. Rev. Lett.* **97**, 042337 (2018).
  - [6] T. J. Proctor, P. A. Knott, and J. A. Dunningham, *Phys. Rev. Lett.* **120**, 080501 (2018).
  - [7] W. Ge, K. Jacobs, Z. Eldredge, A. V. Gorshkov, and M. Foss-Feig, *Phys. Rev. Lett.* **121**, 43604 (2018).
  - [8] Q. Zhuang, Z. Zhang, and J. H. Shapiro, *Physical Review A* **97**, 032329 (2018).
  - [9] E. Polino, M. Riva, M. Valeri, R. Silvestri, G. Corrielli, A. Crespi, N. Spagnolo, R. Osellame, and F. Sciarrino, *Optica* **6**, 288 (2019).
  - [10] V. Giovannetti, S. Lloyd, and L. Maccone, *Phys. Rev. Lett.* **96**, 010401 (2006).
  - [11] B. M. Escher, R. L. De Matos Filho, and L. Davidovich, *Nature Physics* **7**, 406 (2011).
  - [12] V. Giovannetti, S. Lloyd, and L. Maccone, *Nature Photonics* **5**, 222 (2011).
  - [13] H. Yonezawa, D. Nakane, T. A. Wheatley, K. Iwasawa, S. Takeda, H. Arao, K. Ohki, K. Tsumura, D. W. Berry, T. C. Ralph, H. M. Wiseman, E. H. Huntington, and A. Furusawa, *Science* **337**, 1514 (2012).
  - [2] A. A. Berni, T. Gehring, B. M. Nielsen, V. Händchen, M. G. Paris, and U. L. Andersen, *Nature Photonics* **9**, 577 (2015).
  - [15] S. Slussarenko, M. M. Weston, H. M. Chrzanowski, L. K. Shalm, V. B. Verma, S. W. Nam, and G. J. Pryde, *Nature Photonics* **11**, 700 (2017).
  - [16] W. Muessel, H. Strobel, D. Linnemann, D. B. Hume, and M. K. Oberthaler, *Phys. Rev. Lett.* **113**, 103004 (2014).
  - [17] The LIGO Scientific Collaboration, *Nature Physics* **7**, 962 (2011).
  - [18] F. Wolfgramm, A. Cerè, F. A. Beduini, A. Predojević, M. Koschorreck, and M. W. Mitchell, *Phys. Rev. Lett.* **105**, 053601 (2010).
  - [19] B.-B. Li, J. Bilek, U. B. Hoff, L. S. Madsen, S. Forstner, V. Prakash, C. Schäfermeier, T. Gehring, W. P. Bowen, and U. L. Andersen, *Optica* **5**, 850 (2018).
  - [20] J. A. Jones, S. D. Karlen, J. Fitzsimons, A. Ardavan, S. C. Benjamin, G. A. D. Briggs, and J. J. L. Morton, *Science* **324**, 1166 (2009).
  - [21] M. A. Taylor, J. Janousek, V. Daria, J. Knittel, B. Hage, H.-A. Bachor, and W. P. Bowen, *Nature Photonics* **7**, 229 EP (2013).
  - [22] H. Qi, K. Brádler, C. Weedbrook, and S. Guha, *arXiv:1808.01302* (2018).
  - [23] S. Wengerowsky, S. K. Joshi, F. Steinlechner, H. Hübel, and R. Ursin, *Nature* **564**, 225 (2018).
  - [24] S.-K. Liao, W.-Q. Cai, W.-Y. Liu, L. Zhang, Y. Li, J.-G. Ren, J. Yin, Q. Shen, Y. Cao, Z.-P. Li, F.-Z. Li, X.-W. Chen, L.-H. Sun, J.-J. Jia, J.-C. Wu, X.-J. Jiang, J.-F. Wang, Y.-M. Huang, Q. Wang, Y.-L. Zhou, L. Deng, T. Xi, L. Ma, T. Hu, Q. Zhang, Y.-A. Chen, N.-L. Liu, X.-B. Wang, Z.-C. Zhu, C.-Y. Lu, R. Shu, C.-Z. Peng, J.-Y. Wang, and J.-W. Pan, *Nature* **549**, 43 (2017).
  - [25] P. C. Humphreys, M. Barbieri, A. Datta, and I. A. Walmsley, *Phys. Rev. Lett.* **111**, 070403 (2013).
  - [26] P. A. Knott, T. J. Proctor, A. J. Hayes, J. F. Ralph, P. Kok, and J. A. Dunningham, *Phys. Rev. A* **94**, 062312 (2016).
  - [27] T. Baumgratz and A. Datta, *Phys. Rev. Lett.* **116**, 030801 (2016).
  - [28] L. Pezzè, M. A. Ciampini, N. Spagnolo, P. C. Humphreys, A. Datta, I. A. Walmsley, M. Barbieri, F. Sciarrino, and A. Smerzi, *Phys. Rev. Lett.* **119**, 130504 (2017).
  - [29] K. Hammerer, A. S. Sørensen, and E. S. Polzik, *Rev. Mod. Phys.* **82**, 1041 (2010).
  - [30] E. S. Polzik and J. Ye, *Phys. Rev. A* **93**, 021404 (2016).

# Supplemental Materials for Distributed quantum sensing in a continuous variable entangled network

## I. AVERAGED PHASE SHIFT SENSING WITH $\hat{P}_{\text{avg}}$ ESTIMATOR

Our distributed phase sensing scenario is as follows. At each of  $M$  spatially separated locations, an optical phase shift  $\phi_j$  occurs. We are interested in estimating the average phase shift  $\phi_{\text{avg}} = \frac{1}{M} \sum_{j=1}^M \phi_j$ . It is straight-forward to generalize to other linear combinations of the phase shifts, but for the sake of demonstrating the power of the entangled approach it suffices to consider the simple average, where the gain is maximum [S1]. We consider two different approaches: The *separable* scheme where each phase shift is probed individually by squeezed coherent states, and the *entangled* scheme where the  $M$  locations are part of an optical network endowed with a single squeezed coherent state that is distributed among the nodes to serve as an entangled probe. In either case, the phase shifted probes are measured by homodyne detection of their phase quadratures and the results are communicated classically to establish the average.

We furthermore make the following assumptions to simplify the analysis:

1. All the phase shifts are small, giving the small-angle approximation  $\sin \phi \approx \phi$ .
2. All probes in the separable approach are identical, having real-valued displacement amplitude  $\alpha_s$  and squeezing in the phase quadrature with squeezing parameter  $r_s$ . That is, the  $M$  probes are each in the state  $|\psi^{(s)}\rangle = \hat{D}(\alpha_s)\hat{S}(r_s)|0\rangle$ , where  $\hat{D}(\alpha) = \exp(\alpha\hat{a}^\dagger - \alpha^*\hat{a})$  is the displacement operator and  $\hat{S}(r) = \exp(\frac{r}{2}(\hat{a}^{\dagger 2} - \hat{a}^2))$  is the squeezing operator.
3. In the entangled approach, the single initial resource state has real-valued displacement amplitude  $\alpha_e$  and phase squeezing with squeezing parameter  $r_e$ , that is, it is in the state  $|\psi^{(e)}\rangle = \hat{D}(\alpha_e)\hat{S}(r_e)|0\rangle$ . This resource is divided evenly through the network to the  $M$  nodes.
4. The channel losses, quantified by the efficiency parameter  $\eta$ , are identical for the  $M$  channels and they occur entirely prior to the probes reaching the phase samples. In other words, we assume the phase samples themselves and the detection to be lossless. While this assumption is not quite realistic, even in our experiment, it mostly has consequences when keeping track of the number of photons hitting the sample but does not influence the sensitivity as such. In a truly distributed setting, most losses would also happen in the distribution of the resources.

For high-sensitivity estimation of larger phase shifts, these assumptions can still be fulfilled, as long as the local oscillator in the homodyne detector is pre-adjusted to be roughly  $90^\circ$  out of phase with the shifted probe. This rough estimation can be done with just a few initial probings [S2].

### A. General sensitivity for small phase shift

#### 1. Separable scheme

With probe states given as described above, we use the notation defined in Figure S1 to analyse the separable scheme. The phase quadrature of a single mode after channel loss and the phase shift  $\phi_j$  is

$$\hat{p}_j = \left( \sqrt{\eta} \hat{x}_{s,j} + \sqrt{1-\eta} \hat{x}_{\text{vac},j} \right) \sin \phi_j + \left( \sqrt{\eta} \hat{p}_{s,j} + \sqrt{1-\eta} \hat{p}_{\text{vac},j} \right) \cos \phi_j, \quad (\text{S1})$$

where  $\hat{x}_{s,j}, \hat{p}_{s,j}$  are the quadrature operators of the initial squeezed states with mean values  $\langle \hat{x}_{s,j} \rangle = \sqrt{2}\alpha_s$ ,  $\langle \hat{p}_{s,j} \rangle = 0$  and variances  $\langle \Delta \hat{x}_{s,j}^2 \rangle = \frac{1}{2}e^{2r_s}$ ,  $\langle \Delta \hat{p}_{s,j}^2 \rangle = \frac{1}{2}e^{-2r_s}$ , while  $\hat{x}_{\text{vac},j}, \hat{p}_{\text{vac},j}$  are vacuum mode operators admixed through the losses. The expectation value of the rotated phase quadrature is

$$\langle \hat{p}_j \rangle = \sqrt{\eta} \langle \hat{x}_{s,j} \rangle \sin \phi_j = \sqrt{2\eta} \alpha_s \sin \phi_j \approx \sqrt{2\eta} \alpha_s \phi_j. \quad (\text{S2})$$

The phase shift can thus be directly estimated from the measured  $\hat{p}_j$  values. The average phase shift of  $M$  modes,  $\phi_{\text{avg}} = \frac{1}{M} \sum_{j=1}^M \phi_j$ , can then be estimated with the estimator  $\hat{P}_{\text{avg}} = \frac{1}{M} \sum_{j=1}^M \hat{p}_j$ :

$$\langle \hat{P}_{\text{avg}} \rangle \approx \sqrt{2\eta} \alpha_s \phi_{\text{avg}}. \quad (\text{S3})$$

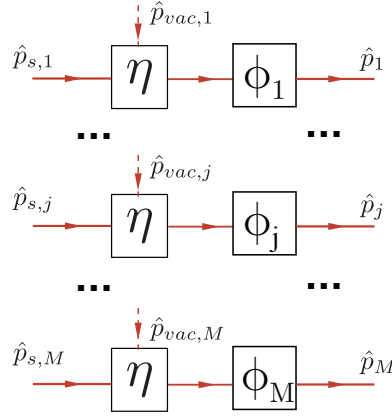


FIG. S1. Phase quadrature notations for analyzing the separable scheme. The amplitude quadrature is defined accordingly.  $\hat{p}_{s,1} \dots \hat{p}_{s,M}$ : operator for the initial squeezed states;  $\hat{p}_{vac,1} \dots \hat{p}_{vac,M}$ : the vacuum operators induced by loss.  $\eta$ : the overall detection efficiency;  $\phi_1 \dots \phi_M$ : the local phase shifts;  $\hat{p}_1 \dots \hat{p}_M$ : phase quadrature of a single mode after channel loss and the phase shift.

The sensitivity of the estimation is defined as the standard deviation which, from standard error propagation analysis, is given by

$$\sigma_s = \frac{\sqrt{\langle \Delta \hat{P}_{\text{avg}}^2 \rangle}}{\left| \partial \langle \hat{P}_{\text{avg}} \rangle / \partial \phi_{\text{avg}} \right|}. \quad (\text{S4})$$

The slope of  $\hat{P}_{\text{avg}}$  versus  $\phi_{\text{avg}}$  is

$$\partial \langle \hat{P}_{\text{avg}} \rangle / \partial \phi_{\text{avg}} \approx \sqrt{2\eta} \alpha_s, \quad (\text{S5})$$

and its variance is

$$\langle \Delta \hat{P}_{\text{avg}}^2 \rangle = \frac{1}{M^2} \left\langle \Delta \left( \sum_{j=1}^M \hat{p}_j \right)^2 \right\rangle = \frac{1}{M^2} \sum_{j=1}^M \langle \Delta \hat{p}_j^2 \rangle \quad (\text{S6})$$

$$= \frac{1}{M^2} \sum_{j=1}^M \left( \sin^2 \phi_j (\eta \langle \Delta \hat{x}_{s,j}^2 \rangle + (1 - \eta) \langle \Delta \hat{x}_{vac,j}^2 \rangle) + \cos^2 \phi_j (\eta \langle \Delta \hat{p}_{s,j}^2 \rangle + (1 - \eta) \langle \Delta \hat{p}_{vac,j}^2 \rangle) \right) \quad (\text{S7})$$

$$= \frac{1}{M^2} \sum_{j=1}^M \left( \frac{\eta e^{2r_s}}{2} \sin^2 \phi_j + \frac{\eta e^{-2r_s}}{2} \cos^2 \phi_j + \frac{1 - \eta}{2} \right). \quad (\text{S8})$$

The second equality comes from the fact that in the separable approach there are no correlations between the modes. Under a stronger bound on the magnitude of the phase shifts,  $\phi_j \ll \sqrt{\langle \Delta \hat{p}_{s,j}^2 \rangle / \langle \Delta \hat{x}_{s,j}^2 \rangle}$ , this expression reduces to

$$\langle \Delta \hat{P}_{\text{avg}}^2 \rangle \approx \frac{1}{M} \left( \eta \langle \Delta \hat{p}_{s,j}^2 \rangle + \frac{1 - \eta}{2} \right) = \frac{\eta e^{-2r_s} + 1 - \eta}{2M}. \quad (\text{S9})$$

Hence, the sensitivity is

$$\sigma_s = \frac{\sqrt{e^{-2r_s} + 1/\eta - 1}}{2\alpha_s \sqrt{M}}. \quad (\text{S10})$$

The average number of photons hitting each sample is

$$N_s = N_{s,\text{coh}} + N_{s,\text{sqz}} = \eta(\alpha_s^2 + \sinh^2 r_s). \quad (\text{S11})$$

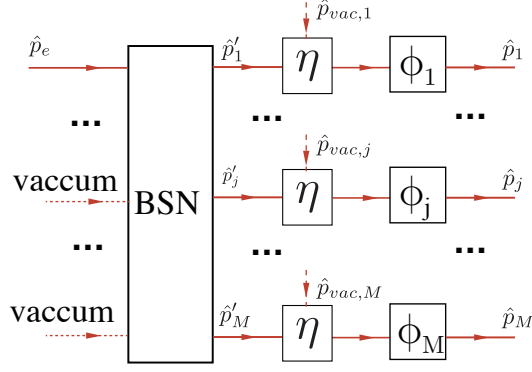


FIG. S2. Phase quadrature notations for analyzing the entangled scheme. The amplitude quadrature is defined accordingly. BSN: beam-splitter network with  $M$  inputs and outputs;  $\hat{p}_e$ : the only non-vacuum input of the BSN;  $\hat{p}'_1 \dots \hat{p}'_M$ : the evenly split  $M$  output of the BSN. All the other notations are the same as Figure S1.

## 2. Entangled scheme

With entangled probes (the notation used in our analysis is summarized in Figure S2), we use the same estimator,  $\hat{P}_{\text{avg}}$ . The individual modes that combine to form the average are, however, now related through the distributed single initial resource  $\hat{p}_e$ :

$$\hat{p}_j = \left( \sqrt{\eta} \hat{x}'_j + \sqrt{1-\eta} \hat{x}_{\text{vac},j} \right) \sin \phi_j + \left( \sqrt{\eta} \hat{p}'_j + \sqrt{1-\eta} \hat{p}_{\text{vac},j} \right) \cos \phi_j, \quad (\text{S12})$$

where the primed mode operators are obtained after symmetric distribution in the beam-splitter network, that is,

$$\hat{x}_e = \frac{1}{\sqrt{M}} \sum_{j=1}^M \hat{x}'_j, \quad \hat{p}_e = \frac{1}{\sqrt{M}} \sum_{j=1}^M \hat{p}'_j. \quad (\text{S13})$$

The mean value of the estimator is

$$\langle \hat{P}_{\text{avg}} \rangle = \frac{1}{M} \sum_{j=1}^M \langle \hat{p}_j \rangle \approx \frac{\sqrt{\eta}}{M} \sum_{j=1}^M \langle \hat{x}'_j \rangle \phi_j = \sqrt{\frac{2\eta}{M}} \alpha_e \phi_{\text{avg}}. \quad (\text{S14})$$

The variance is

$$\begin{aligned} \langle \Delta \hat{P}_{\text{avg}}^2 \rangle &= \frac{1}{M^2} \left\langle \Delta \left( \sum_{j=1}^M \hat{p}_j \right)^2 \right\rangle \\ &\approx \frac{\eta}{M^2} \left\langle \Delta \left( \sum_{j=1}^M \hat{x}'_j \phi_j \right)^2 \right\rangle + \frac{\eta}{M^2} \left\langle \Delta \left( \sum_{j=1}^M \hat{p}'_j \right)^2 \right\rangle + \frac{1-\eta}{M^2} \left\langle \Delta \left( \sum_{j=1}^M \hat{p}_{\text{vac},j} \right)^2 \right\rangle \\ &\approx \frac{\eta}{M^2} \left\langle \Delta \left( \sum_{j=1}^M \hat{p}'_j \right)^2 \right\rangle + \frac{1-\eta}{M^2} \sum_{j=1}^M \langle \hat{p}_{\text{vac},j}^2 \rangle \\ &= \frac{\eta}{M^2} M \langle \Delta \hat{p}_e^2 \rangle + \frac{1-\eta}{M^2} \sum_{j=1}^M \langle \hat{p}_{\text{vac},j}^2 \rangle \\ &= \frac{\eta e^{-2r_e} + 1 - \eta}{2M}. \end{aligned} \quad (\text{S15})$$

In the second line, we made use of the fact that there are no correlations between  $\hat{x}$  and  $\hat{p}$  quadratures for the given probe state in our entangled scheme as well as the small angle approximation  $\cos(\phi_j) \approx 1$ ,  $\sin(\phi_j) \approx \phi_j$ . In the third

line, we further tightened the small angle approximation by taking a  $\tilde{\phi}$  such that for all  $j$ ,  $|\phi_j| < \tilde{\phi}$  and assuming

$$\begin{aligned}\tilde{\phi}^2 \left\langle \Delta \left( \sum_{j=1}^M \hat{x}'_j \right)^2 \right\rangle &\ll \left\langle \Delta \left( \sum_{j=1}^M \hat{p}'_j \right)^2 \right\rangle \\ \Rightarrow \tilde{\phi}^2 &\ll \frac{\langle \Delta \hat{p}_e^2 \rangle}{\langle \Delta \hat{x}_e^2 \rangle} \\ \Rightarrow \tilde{\phi} &\ll e^{-2r_e}.\end{aligned}\tag{S16}$$

This approximation gives a sensitivity for the entangled approach of

$$\sigma_e = \frac{\sqrt{\langle \Delta \hat{P}_{\text{avg}}^2 \rangle}}{|\partial \langle \hat{P}_{\text{avg}} \rangle / \partial \phi_{\text{avg}}|} = \frac{\sqrt{e^{-2r_e} + 1/\eta - 1}}{2\alpha_e}.\tag{S17}$$

Note that this, in contrast with the separable approach, does not depend on the number of modes  $M$ . The sensitivity is therefore the same as the sensitivity for a single mode with the same resource state - but in the single mode case the sample would of course be exposed to  $M$  times as many photons. The average number of photons hitting each sample in the distributed, entangled scheme is

$$N_e = N_{e,\text{coh}} + N_{e,\text{sqz}} = \frac{\eta}{M}(\alpha_e^2 + \sinh^2 r_e).\tag{S18}$$

## B. Optimized parameters and sensitivities

### 1. Entangled scheme

With the sensitivities given by eqs. (S10) and (S17), we wish to find the values for the displacement amplitudes and squeezing parameters that optimize the sensitivity for a fixed photon number on the sample. This problem can be solved with Lagrangian multipliers, using the constraint  $N_{s,e} - N = 0$ , where  $N$  is the photon number to be held fixed during optimization. The total photon number of the resource state(s) before loss is then  $N_{\text{tot}} = MN/\eta$ .

The Lagrange function for the entangled scheme is

$$\mathcal{L}_e(\alpha_e, r_e, \lambda) = \sigma_e + \lambda(N_e - N)\tag{S19}$$

$$= \frac{\sqrt{e^{-2r_e} + 1/\eta - 1}}{2\alpha_e} + \lambda \frac{\eta}{M}(\alpha_e^2 + \sinh^2 r_e) - \lambda N,\tag{S20}$$

and the equations for the stationary point of the Lagrangian become

$$0 = \nabla_{\alpha_e} \mathcal{L}_e = -\frac{\sqrt{e^{-2r_e} + 1/\eta - 1}}{2\alpha_e^2} + \frac{2\lambda\eta\alpha_e}{M},\tag{S21}$$

$$0 = \nabla_{r_e} \mathcal{L}_e = -\frac{e^{-2r_e}}{2\alpha_e \sqrt{e^{-2r_e} + 1/\eta - 1}} + \frac{2\lambda\eta \cosh r_e \sinh r_e}{M},\tag{S22}$$

$$0 = \nabla_{\lambda} \mathcal{L}_e = \frac{\eta}{M}(\alpha_e^2 + \sinh^2 r_e) - N.\tag{S23}$$

After some manipulation, the solutions can be expressed as

$$e^{2r_e} = \frac{\Lambda_M - \eta}{1 - \eta},\tag{S24}$$

$$\alpha_e^2 = N_{\text{tot}} - \sinh^2 r_e = N_{\text{tot}} - \frac{e^{2r_e} + e^{-2r_e} - 2}{4} = \frac{MN}{\eta} - \frac{(\Lambda_M - 1)^2}{4(1 - \eta)(\Lambda_M - \eta)},\tag{S25}$$

with  $\Lambda_M = \sqrt{1 + 4MN(1 - \eta)}$ . The optimal photon number ratio is



$$\mu_e = \frac{N_{e,\text{sqz}}}{N} = \frac{\sinh^2 r_e}{N_{\text{tot}}} = \frac{\eta(\Lambda_M - 1)^2}{4MN(1 - \eta)(\Lambda_M - \eta)}, \quad (\text{S26})$$

and the optimal sensitivity obtained with these parameters becomes

$$\sigma_e^{\text{opt}} = \frac{1}{2MN} \sqrt{\frac{MN(1 - \eta) + \eta(\Lambda_M + 1)/2}{1 + \eta/(MN)}}, \quad (\text{S27})$$

which for  $\eta = 1$  reduces to  $\sigma_e^{\text{opt}}(\eta = 1) = \frac{1}{2MN} \sqrt{\frac{MN}{MN+1}}$ . This sensitivity exhibits Heisenberg scaling in both photon number (due to the squeezing) and mode number (due to the entanglement).

## 2. Separable scheme

Doing the same derivation for the separable scheme, that is, starting from the Lagrange function  $\mathcal{L}_s(\alpha_s, r_s, \tilde{\lambda}) = \sigma_s + \tilde{\lambda}(N_s - N)$ , results in the following optimal parameters for squeezing and displacement:

$$e^{2r_s} = \frac{\Lambda_1 - \eta}{1 - \eta}, \quad (\text{S28})$$

$$\alpha_s^2 = \frac{N_{\text{tot}}}{M} - \sinh^2 r_s = \frac{N}{\eta} - \frac{(\Lambda_1 - 1)^2}{4(1 - \eta)(\Lambda_1 - \eta)}, \quad (\text{S29})$$

with  $\Lambda_1 = \sqrt{1 + 4N(1 - \eta)}$ , and a corresponding photon number ratio

$$\mu_s = \frac{N_{s,\text{sqz}}}{N} = \frac{M \sinh^2 r_s}{N_{\text{tot}}} = \frac{\eta(\Lambda_1 - 1)^2}{4N(1 - \eta)(\Lambda_1 - \eta)}. \quad (\text{S30})$$

Finally, the optimal sensitivity becomes

$$\sigma_s^{\text{opt}} = \frac{1}{2\sqrt{MN}} \sqrt{\frac{N(1 - \eta) + \eta(\Lambda_1 + 1)/2}{1 + \eta/N}}, \quad (\text{S31})$$

which for  $\eta = 1$  reduces to  $\sigma_s^{\text{opt}}(\eta = 1) = \frac{1}{2\sqrt{MN}} \sqrt{\frac{N}{N+1}}$ , thus no longer showing Heisenberg scaling in the mode number. The result enable us to obtain the simulation result in Fig 1c and 1d in the main text, and the optimal  $\mu$  and corresponding squeezing rated need to get the optimal  $\mu$  is shown in Fig. S3.

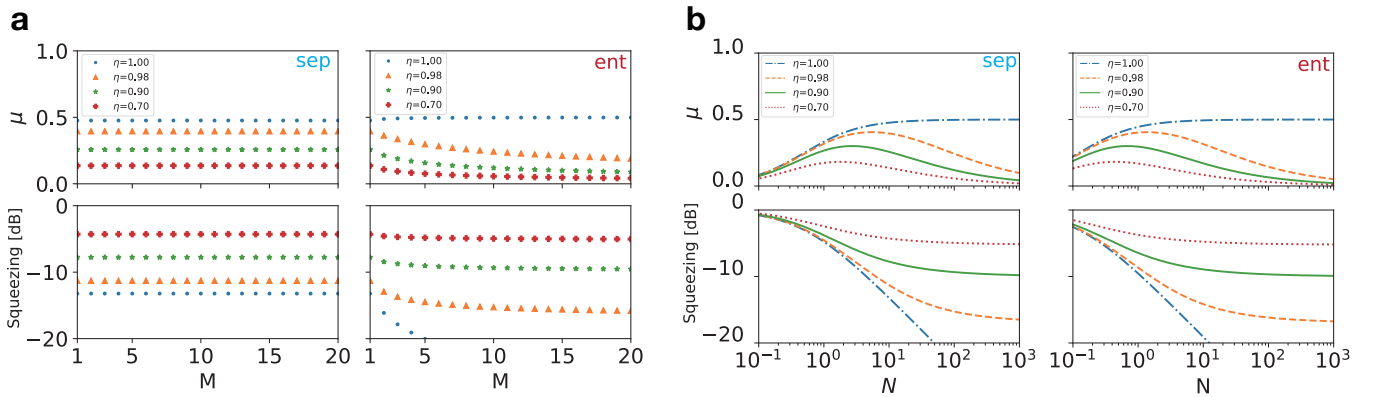


FIG. S3. **a** and **b**: Optimized squeezed photon number ratio  $\mu$  and squeezing degrees  $\eta e^{-2r} + (1 - \eta)$  for the Fig. 1c and 1d in the main text, respectively. Sep, the separable approach; Ent, the entangled approach.

## II. ULTIMATE SENSITIVITY LIMIT

In this section, we show that the sensitivity of  $\phi_{\text{avg}}$  sensing with our entangled approach is directly related to the photon number variance of the input state of the BSN. Then we discuss the optimal input state for our entangled approach, giving the optimal Quantum Cramér-Rao Bound (QCRB), plotted in Fig 3a in the main text.

We denote a general unbiased local estimator for the phase shift  $\phi_j$  in the individual channels as  $\hat{\phi}_j$ . Note that in the previous section the focus was on the special case of  $\hat{\phi}_j = \hat{p}_j$ . With an initial state  $\hat{\rho}$ , the state evolution caused by the parameters is described by the overall generator of the  $M$  phase shifts,  $\hat{U}(\phi_1, \dots, \phi_M) = \exp[-i\hat{\mathbf{n}} \cdot (\phi_1, \dots, \phi_M)]$ , where  $\hat{\mathbf{n}} = (\hat{n}_1, \dots, \hat{n}_M)$  is a vector of the  $M$  photon number operators. The sensitivity for the multi-parameter estimation is given by a covariance matrix  $\mathbf{K}$  whose elements are defined as  $K_{i,j} = \text{Cov}(\hat{\phi}_i, \hat{\phi}_j)$  and it is lower bounded by the inverse of the quantum Fisher information matrix  $\mathbf{F}_Q$  [S3, S4].  $\mathbf{F}_Q$ , which decide the ultimate sensitivity limit of multi-parameter sensing, is only a function of  $\hat{\rho}$  itself once the parameters to sense are decided. Moreover,  $\mathbf{F}_Q$  is further bounded by the covariance matrix of the Hamiltonian  $\mathbf{\Gamma}$ , defined below. These bounds can be clearly shown by the following inequality [S5]:

$$\mathbf{K} \geq \mathbf{F}_Q^{-1} \geq \frac{1}{4} \mathbf{\Gamma}^{-1} \quad (\text{S32})$$

with

$$\mathbf{\Gamma} = \frac{1}{2} (\langle \hat{n}_i \hat{n}_j \rangle_{\hat{\rho}} + \langle \hat{n}_j \hat{n}_i \rangle_{\hat{\rho}}) - \langle \hat{n}_i \rangle_{\hat{\rho}} \langle \hat{n}_j \rangle_{\hat{\rho}}. \quad (\text{S33})$$

The second inequality in Eq. (S32) is saturated when  $\hat{\rho}$  is a pure state. From the matrix inequalities, for a general phase sensing task  $\phi_{\mathbf{M}, \mathbf{w}} = \sum_{j=1}^M w_j \phi_j$  denoted by the weight vector  $\mathbf{w} = (w_1, \dots, w_M)$  and with estimator  $\hat{\phi}_{\mathbf{M}, \mathbf{w}} = \sum_{j=1}^M w_j \hat{\phi}_j$ , it follows that

$$\langle \Delta \hat{\phi}_{\mathbf{M}, \mathbf{w}}^2 \rangle = \mathbf{w}^T \mathbf{K} \mathbf{w} \geq \mathbf{w}^T \mathbf{F}_Q^{-1} \mathbf{w} \geq \frac{1}{4} \mathbf{w}^T \mathbf{\Gamma}^{-1} \mathbf{w} \quad (\text{S34})$$

holds for any  $\mathbf{w}$ .

Next, we show that the ultimate sensitivity of our entangled approach is bounded by the photon number variance of the single squeezed input state of the BSN, which in our experiment is evenly distributed into 4 identical probes. Furthermore, we are considering the average phase shift with weight vector  $\mathbf{w}_{\text{avg}} = (1/4, \dots, 1/4)$ . The identical property of the probes gives  $\mathbf{\Gamma}$  the form

$$\mathbf{\Gamma} = \begin{pmatrix} V & C & C & C \\ C & V & C & C \\ C & C & V & C \\ C & C & C & V \end{pmatrix}, \quad (\text{S35})$$

where we respectively denote diagonal and off-diagonal terms as  $V = \langle \hat{n}_j \hat{n}_j \rangle - \langle \hat{n}_j \rangle \langle \hat{n}_j \rangle$  and  $C = \langle \hat{n}_j \hat{n}_k \rangle - \langle \hat{n}_j \rangle \langle \hat{n}_k \rangle$  for  $j, k = 1 \dots 4$ . Using the above formalism we can then state a lower bound for the sensitivity of the average phase shift as:

$$\langle \Delta \hat{\phi}_{\text{avg}}^2 \rangle = \frac{1}{4^2} \sum_{i,j=1}^4 \text{Cov}(\hat{\phi}_i, \hat{\phi}_j) \geq \frac{1}{4} \mathbf{w}_{\text{avg}}^T \mathbf{\Gamma}^{-1} \mathbf{w}_{\text{avg}} \quad (\text{S36})$$

For our entangled approach,  $V$  and  $C$  in Eq. (S36) can be directly calculated through the input-output relations of the BSN (Eq. (S43) in Sec. III) and using  $\hat{n}_j = \hat{b}_j^\dagger \hat{b}_j$ , though we here take a simpler approach and relate  $\langle \phi_{\text{avg}}^2 \rangle$  to the photon number variance before splitting. Noting the fact that all the other inputs of the BSN are vacuum, it is direct to check the following equation holds for any input state:

$$\langle \Delta \hat{n}^2 \rangle = \langle \Delta (\hat{n}_1 + \hat{n}_2 + \hat{n}_3 + \hat{n}_4)^2 \rangle = 16 \mathbf{n}_{\text{avg}}^T \mathbf{\Gamma} \mathbf{n}_{\text{avg}}, \quad (\text{S37})$$

where  $\hat{n}$  is the photon number operator of the non-vacuum input mode of the BSN, assuming it go through a lossy channel with the same efficiency  $\eta$  as it is for our entangled approach. The symmetric form of  $\mathbf{\Gamma}$  in Eq. (S35) leads to the equality

$$(\mathbf{n}_{\text{avg}}^T \mathbf{\Gamma} \mathbf{n}_{\text{avg}})^{-1} = \frac{1}{16} \mathbf{n}_{\text{avg}}^T \mathbf{\Gamma}^{-1} \mathbf{n}_{\text{avg}} \quad (\text{S38})$$

From Eq. (S36-S38), a lower bound of the estimation variance for the entangled approach is

$$\langle \Delta \hat{\phi}_{\text{avg}}^2 \rangle \geq \frac{1}{4 \langle \Delta \hat{n}^2 \rangle}. \quad (\text{S39})$$

An explicit expression for  $\langle \Delta \hat{n}^2 \rangle$  for an arbitrary Gaussian state was derived in Ref. [S6, S7] to bound the sensitivity of a single parameter phase sensing. In a slightly rewritten form, this expression is

$$\langle \Delta \hat{n}^2 \rangle = \frac{e^{2r'}}{2N_{th} + 1} \alpha^2 + \frac{(2N_{th} + 1)^2 (e^{4r'} + e^{-4r'} - 2)}{(4N_{th} + 2)^2 + 4} \quad (\text{S40})$$

with

$$N_{th} = \frac{1}{2} [(\eta e^{-2r} + 1 - \eta)(\eta e^{2r} + 1 - \eta) - 1] \quad (\text{S41})$$

being an effective thermalization of the mixed state resulting from channel loss, and

$$r' = \frac{1}{4} \log \left[ \frac{\eta e^{2r} + 1 - \eta}{\eta e^{-2r} + 1 - \eta} \right] \quad (\text{S42})$$

being the effective squeezing parameter after channel loss. With Eq. (S39-S42), we fix the average photon number after channel loss on each sample  $N = \eta(\alpha^2 + \sinh^2 r)/4$  and maximize  $\langle \Delta \hat{n}^2 \rangle$  by tuning the ratio between  $\alpha$  and  $r$  at our given overall detection efficiency. The sensitivity obtained from the optimized  $\langle \Delta \hat{n}^2 \rangle$  is plotted in Fig. 3a in the main text. We note that at our detection efficiency the optimized result is obtained at  $\alpha = 0$  (no coherent component), but as the efficiency is further decreased a coherent component will be needed to reach the optimal  $\langle \Delta \hat{n}^2 \rangle$ . Moreover, with  $\eta \neq 1$ , the optimal measurement is in general non-Gaussian [S8, S9].

### III. PREPARATION OF ENTANGLED PROBES

The entangled probes are prepared in two steps. First, we generate a squeezed coherent state, denoted as the squeezed probe (SP), by an optical parametric oscillator (OPO). Second, we send the SP through a beam-splitter network (BSN) to generate 4 entangled probes. We define the mode of the SP to be a narrow sideband at 3 MHz, since this is region where we have high squeezing quality.

#### A. Generation of squeezed probes with OPO

The laser source for the experiment is an amplified NKT Photonics X-15 fibre laser operating at 1550 nm. Most of the light is used for pumping a second harmonic generation (SHG) cavity (same design as the OPO described below) to produce 775 nm light to act as the OPO pump. The rest is used for the local oscillator and the probe and lock beams. As shown in Fig. S4, we use a bow-tie shaped OPO with a periodically poled potassium titanyl phosphate (PPKTP) crystal to generate the SP by type-0 parametric down conversion. The bandwidth of the cavity is 8.0 MHz half width half maximum (HWHM) and the OPO pump power threshold is 850 mW. The 775 nm pump, which for the measurements presented here varied between 150 mW and 350 mW, is coupled through the dichroic curved cavity mirrors and dumped after passing the crystal. A 3.6 mW coherent beam at 1550 nm, weakly phase-modulated by an electro-optic modulator (EOM) at 3 MHz and 28.7 MHz, is coupled into the OPO in the counter-propagating direction through a high reflectivity mirror (HR) with a transmittance of about 100 ppm. This beam is used to lock the cavity by the Pound–Drever–Hall technique with the 28.7 MHz side band and the resonant detector D1. All cavity and phase locks in the experiment are handled by Red Pitaya FPGA boards running the PyRPL lockbox software [S10].

The reflection from the HR mirror is re-coupled into the forward-propagating mode of the OPO with a  $0^\circ$  mirror to serve as the carrier of the sideband mode that defines our probe state. A variable attenuator (Att.) is inserted to control the optical power. In the OPO, the forward-propagating beam is squeezed by the parametric process and coupled out through a 10% transmissive out coupling mirror (light gray in Fig. S4). A half-wave plate ( $\lambda/2$ ) and a polarization beam-splitter (PBS) is used to tap around 1% of the OPO output towards detector D2 to lock the phase between the carrier and the pump for de-amplification. As a result, the carrier is squeezed in the amplitude quadrature, leading to squeezing of the phase quadrature of the probe in the 3 MHz modulated sideband frequency mode since the sideband is encoded by phase modulation.

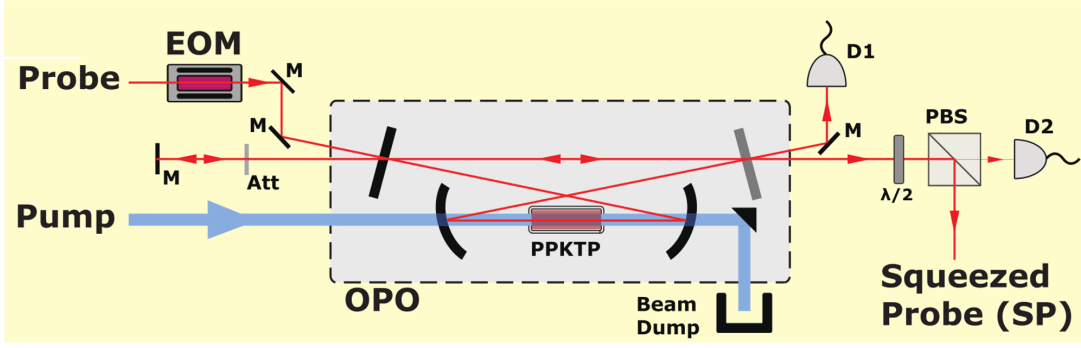


FIG. S4. Squeezed probe (SP) preparation with OPO. M, high reflectively mirror; EOM, electro-optic modulator; Att, attenuator; D1, resonant detector for cavity lock; D2, high gain detector for OPO gain lock.

### B. Generation and detection of entangled probes

The detailed experimental setup is shown in Fig. S5. It is essentially a multi-port version of a squeezed-light-enhanced polarization interferometer [S11]. We create four entangled probes by sending the squeezed probe, SP, through a BSN consisting of three 50:50 beam-splitters. Prior to this, the SP is spatially combined on a PBS with a strong beam (LO) which will act as the local oscillator for all four modes. The LO phase is locked to either the  $\hat{p}$  or  $\hat{x}$  quadrature of the SP by tapping  $\sim 1\%$  towards a polarization-based homodyne detection setup, the output of which is used to control a piezo-mounted mirror in the LO path. In each of the four modes, the phase between LO and SP can be further controlled by a  $\lambda/4$  and a  $\lambda/2$  wave plate. The  $\lambda/4$  plates change the LO and SP into left-hand and right-hand circular polarization, respectively. The  $\lambda/2$  plates introduce phase shifts between SP and LO and play two roles: First, they are used to synchronize the phases for the entangled probes by compensating the phase difference induced by 50:50 beam splitters. Second, they are used to simulate the phase samples, that is, the imposed phases  $\phi_1, \dots, \phi_4$ . For details, see section IV A. Finally, the four outputs are measured on homodyne detectors.

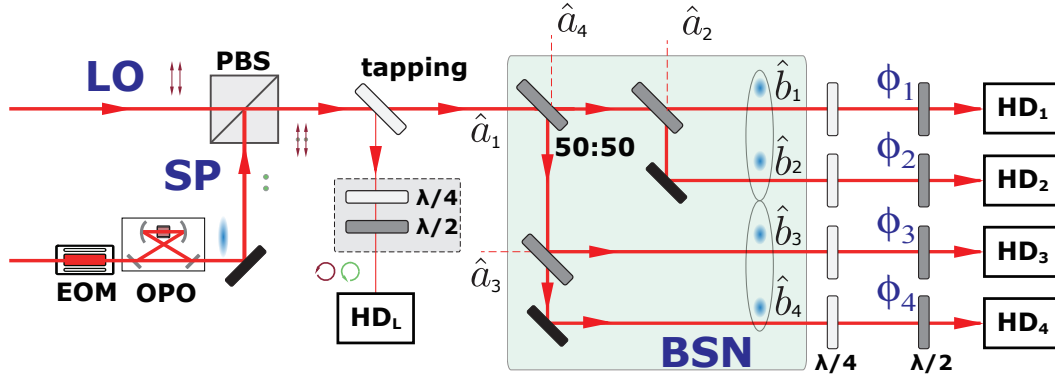


FIG. S5. Detailed experimental setup and the input-output relationship of the beam splitter network (BSN). The input modes  $\hat{a}_1$  to  $\hat{a}_4$  with s-polarization are transferred into the output modes  $\hat{b}_1$  to  $\hat{b}_4$ . Here, only  $\hat{a}_1$  is a squeezed coherent state operator.  $\hat{a}_2$  to  $\hat{a}_4$  are vacuum operators. By tuning the wave plates at each output of the BSN,  $\hat{b}_1$  to  $\hat{b}_4$  are set to circular polarization.

#### 1. Homodyne detection and data acquisition

All five homodyne detection setups use the same scheme, illustrated in Fig. S6a. The circularly polarized SP and LO interfere after the PBS. The optical power of the LO is about 3 mW on each HD and it detects a SP of about 10 nW. The output of the detector is electronically split into AC and DC parts with a bias-tee of about 100 kHz. The AC signal,  $V_{ac}$ , is used for phase sensing. It includes the 3 MHz side-band, but filters out the carrier at DC and the side-band for cavity locking at 28.7 MHz with a low pass filter at around 14 MHz. The DC signal,  $V_{dc}$ , detects the carrier. It is used for phase locking and phase calibration (see section IV B).

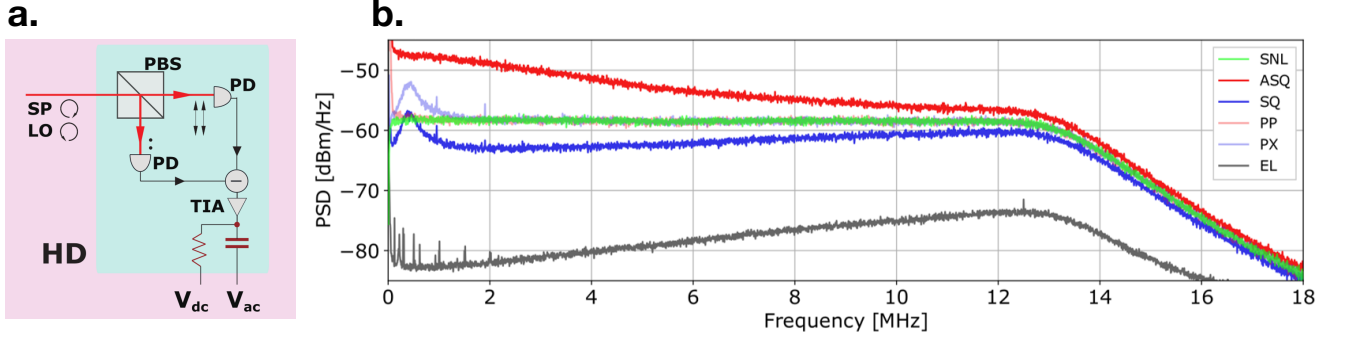


FIG. S6. **a.** The circular polarized SP and local oscillator (LO) are projected into p- or s-polarization by a PBS, and detected with a balanced photo-detector. The output voltage of the detector photo diodes is separated into DC–100 kHz output  $V_{dc}$  and 100 kHz–14 MHz output  $V_{ac}$ . PD, photo diode; TIA, trans-impedance amplifier. **b.** Power spectral densities (PSDs). SNL, shot-noise limit; ASQ, anti-squeezing; SQ, squeezing; PX and PP, probe noise in X and P quadrature respectively, measured by blocking pump; EL, electronic noise of the data acquisition system, measured by blocking both SP and the LO.

The  $V_{ac}$  outputs of HD1 to HD4 are sent to a 4-channel oscilloscope (LeCroy HDO6034), which acquires time-voltage traces of 200  $\mu$ s with a 50 MHz sampling rate. The power spectral densities (PSDs) of the individual HD outputs and the averaged output is obtained by Fast Fourier Transform (FFT) on a computer. Fig. S6b shows PSDs for the averaged voltage of the 4 HDs in different experimental conditions with no modulation from the EOM. All the PSDs in Fig. S6b are the averaged result of 400 oscilloscope measurements. To show the signal-to-noise ratio of the data acquisition system, we measure the PSDs of the shot noise level (SNL, measured when SP is blocked) and electronic noise (EL, measured when both SP and LO are blocked). The result is shown in green and dark grey traces in Fig. S6b. We see that the electronic noise clearance is about 23 dB at the 3 MHz side band, which corresponds to about 0.5% effective loss in detection efficiency. We will discuss the other PSDs shown in Fig. S6b in the following subsection.

## 2. Input-output relations of the BSN

The BSN we use in the experiment is shown in Figure S5. The only non-vacuum input mode  $\hat{a}_1$  is the SP, whose mode operator is  $\hat{a}_1 = \hat{S}^\dagger(r)\hat{a}\hat{S}(r) + \alpha$  in the Heisenberg picture, with  $\hat{a}$  being the annihilation operator of the OPO input at 3 MHz and the real-valued  $\alpha$  being the effective coherent excitation of the mode after modulation by the EOM and de-amplification in the OPO. All the other input modes  $\hat{a}_2$ ,  $\hat{a}_3$  and  $\hat{a}_4$  are vacuum modes. The output modes of the BSN,  $\hat{b}_j$  can be explicitly written as:

$$\begin{aligned}\hat{b}_1 &= \frac{1}{2}\sqrt{\eta}(\hat{a}_1 - i\hat{a}_4 + \sqrt{2}i\hat{a}_2) + \sqrt{1-\eta}\hat{a}_{vac,1} \\ \hat{b}_2 &= \frac{1}{2}\sqrt{\eta}(\hat{a}_1 - i\hat{a}_4 - \sqrt{2}i\hat{a}_2) + \sqrt{1-\eta}\hat{a}_{vac,2} \\ \hat{b}_3 &= \frac{1}{2}\sqrt{\eta}(\hat{a}_1 + i\hat{a}_4 + \sqrt{2}i\hat{a}_3) + \sqrt{1-\eta}\hat{a}_{vac,3} \\ \hat{b}_4 &= \frac{1}{2}\sqrt{\eta}(\hat{a}_1 + i\hat{a}_4 - \sqrt{2}i\hat{a}_3) + \sqrt{1-\eta}\hat{a}_{vac,4}.\end{aligned}\tag{S43}$$

Here we have introduced an identical overall efficiency  $\eta$  and vacuum mode operator  $\hat{a}_{vac,j}$  for  $j = 1 \dots 4$ . Although the various inefficiencies occur at different points in the experiment, for simplicity we have assumed (as in section I) that they all occur after the distribution of the probes in the BSN and that they are identical for the four channels. Experimentally, we use eight variable irises before the PDs of all four HDs to equalize the overall detection efficiency.

## 3. Overall detection efficiency estimation

The loss budget of our experiment setup is as follows: the escape efficiency of the OPO  $\sim 95\%$ ; the quantum efficiency of the photo diodes in HD  $\sim 98\%$ ; the imperfection of the mode matching between SP and LO  $\sim 90\%$ ; the



electronic noise of the homodyne detection  $\sim 99\%$ ; the efficiency introduced by tapping for phase locking  $\sim 97\%$  and the efficiency of all optics between OPO output and the PD of the HD  $\sim 92\%$ . The loss budget of the experiment system gives an estimation of the overall detection efficiency of  $\eta \sim 74\%$ .

We also estimate the overall detection efficiency by measuring the squeezing/anti-squeezing degrees (notated with  $v_{sq}^2$  and  $v_{asq}^2$ ) for the entangled approach at 3 MHz. Since

$$\begin{aligned} v_{sq}^2 &= \eta e^{-2r_e} + (1 - \eta) \\ v_{asq}^2 &= \eta e^{2r_e} + (1 - \eta), \end{aligned} \quad (\text{S44})$$

we can calculate  $\eta$  and  $r_e$  with measured  $v_{sq}^2$  and  $v_{asq}^2$ . The overall efficiency estimated with 5 different pump powers to the OPO is  $\eta = 73.5\% \pm 1.5\%$ . This result coincide with the loss budget estimation, and we use this result to theoretically calculate the sensitivity.

For the separable approach, where the BSN is removed, the overall efficiency is  $\sim 1.5\%$  higher. However, we compensate this by tapping more to the lock detector D2 in Figure S4 so the separable approach has similar efficiency to that of the entangled approach.

#### 4. Entanglement characterization of the probes

The squeezing degree for each individual output mode will not be better than 3/4 shot noise due to the splitting of the SP in the BSN. However, the squeezing of SP is converted into entanglement between all the probes. By joint measurement of the 4 probes (simply averaging the voltage from the four HDs), we can recover the squeezing degree of the SP: From Eq. (S43), the joint measurement recovering the squeezing of SP is simply the sum of the four HD<sub>1-4</sub> outputs. The recovered squeezed and anti-squeezed quadratures are shown as SQ (blue) and ASQ (red) in Fig. S6b. We see the joint measurement gives about 4.8 dB of squeezing at the 3 MHz side band frequency. The additional noise seen below 2 MHz is due to technical noise from our laser. As a calibration of the noise of the probe before the parametric process, we measure the PSDs of  $\hat{X}$  and  $\hat{P}$  quadrature by blocking the pump of our OPO, and the result is shown with PX (light blue) and PP (light red) in Fig. S6b (noting that here we refer to the amplitude/phase quadrature of the carrier of the SP since there is no side-band). We see the technical noise of both  $\hat{X}$  and  $\hat{P}$  quadrature decreases as the frequency increases and overlap with the SNL when the frequency is above 1.8 MHz. Therefore, in our estimation of the overall detection efficiency at the side band frequency (3 MHz), we ignore contributions from technical noise of the laser.

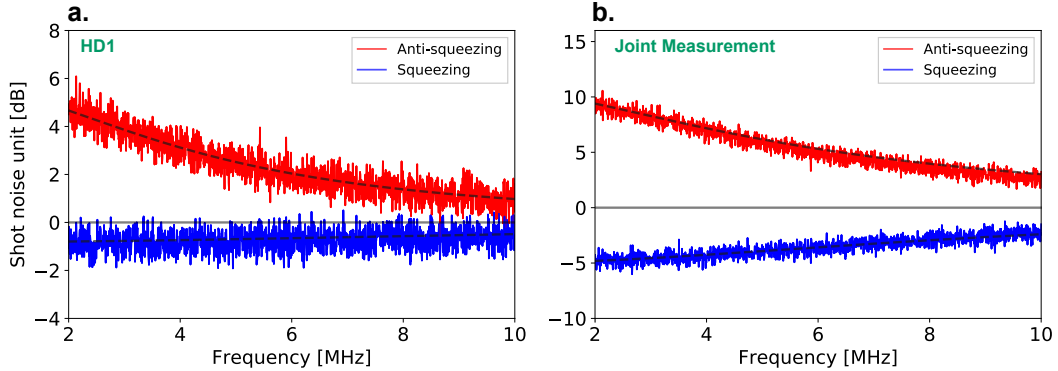


FIG. S7. **a.** Squeezing and anti-squeezing spectra for a single distributed spatial mode obtained from HD<sub>1</sub>. **b.** Squeezing and anti-squeezing spectra from joint measurement. Dashed lines: spectra predicted by theory.

With the measurement described in Fig. S6b, we can get the squeezing/anti-squeezing degree in SNL units. Fig. S7a and b shows the squeezing and anti-squeezing of an individual channel (HD<sub>1</sub>) and that from the joint measurement, respectively. The dashed lines show the squeezing and anti-squeezing predicted by [S12]

$$S^{\pm}(f) = 1 \pm \frac{4\eta\sqrt{P/P_{th}}}{(1 \mp \sqrt{P/P_{th}})^2 + (f/f_{cav})^2}, \quad (\text{S45})$$

where  $S^{-}(f)$  and  $S^{+}(f)$  denotes the squeezing and anti-squeezing spectrum,  $\eta = 0.735$  is the estimated overall detection efficiency,  $f_{cav} = 8.0$  MHz is the HWHM of the OPO cavity and  $P_{th} = 850$  mW is the threshold of the

OPO. In this measurement,  $P = 300$  mW pump power is used. Here both  $f_{cav}$  and  $P_{th}$  are obtained from independent measurements.

We quantitatively verify the entanglement of the probes by reconstructing the covariance matrix of the 4 modes. As we do not expect correlations between  $\hat{x}$  and  $\hat{p}$  quadratures, we only experimentally reconstruct  $M_x = \text{Cov}(\hat{x}_j, \hat{x}_k)$  and  $M_p = \text{Cov}(\hat{p}_j, \hat{p}_k)$  for  $j, k = 1$  to 4 at around 3 MHz. After balancing the length of cables from HD<sub>1-4</sub> to the oscilloscope, we digitally filter the recorded traces by a 50 kHz band pass filter centered around 3 MHz, and measure  $M_x$  and  $M_p$ , respectively. The covariance matrices in shot noise units from the average of 400 oscilloscope measurements are:

$$M_x = \begin{pmatrix} 0.83 & -0.18 & -0.17 & -0.19 \\ - & 0.84 & -0.16 & -0.18 \\ - & - & 0.83 & -0.18 \\ - & - & - & 0.82 \end{pmatrix} \quad M_p = \begin{pmatrix} 3.0 & 1.9 & 1.9 & 2.0 \\ - & 2.8 & 1.8 & 1.9 \\ - & - & 2.8 & 1.9 \\ - & - & - & 3.0 \end{pmatrix}, \quad (\text{S46})$$

where symmetric elements are not shown. We show the entanglement property of the probes by calculating the logarithmic negativity  $\mathcal{N}(\hat{\rho})$  between them, where  $\mathcal{N}(\hat{\rho}) > 0$  is a sufficient condition for entanglement [S13]. For a Gaussian state this can be obtained through the symplectic eigenvalues of the partially transposed covariance matrix, so that  $\mathcal{N}(\rho) = \sum_k f(\tilde{v}_k)$ , where  $\tilde{v}_k$  are the symplectic eigenvalues and  $f(x) = -\log_2(x)$  for  $x < 1$  and 0 otherwise. By constructing the full  $M_{x,p}$  covariance matrix from  $M_x$  and  $M_p$ , we find that for any two, three or four modes the value of  $\mathcal{N}(\hat{\rho})$  is within the range of  $0.20 \pm 0.02$ ,  $0.33 \pm 0.02$  and  $0.51 \pm 0.02$  respectively, confirming the presence of quadrature entanglement across all mode combinations.

#### IV. PHASE CONTROL AND CALIBRATION

In this section we first calculate the interference at the two photo diodes of the HD in Fig. S6. The result shows that the phase between SP and LO can be controlled by rotating the  $\lambda/2$  wave plates. After that, we describe the phase calibration procedure and result in our experiment. With the phase calibration result, we can control the phase  $\phi_j$  for  $j = 1 \dots 4$  (and therefore  $\phi_{\text{avg}}$ ) by rotating the  $\lambda/2$  wave plates to a specific position.

##### A. Phase control with $\lambda/2$ wave plates

The LO with p polarization and OPO output with s polarization are combined by the PBS in Fig. S5, and the Jones vector after the PBS is

$$J_{in} = \begin{bmatrix} E_{LO} \cdot e^{-i\phi_{LO}} \\ E_{SP} \cdot e^{-i\phi_{SP}} \end{bmatrix}, \quad (\text{S47})$$

where  $E_{LO} \cdot e^{-i\phi_{LO}}$  is the LO and  $E_{SP} \cdot e^{-i\phi_{SP}}$  is the OPO output (squeezed probe). The Jones Matrix for a wave plate is [S14]

$$M_{wp} = \begin{bmatrix} \cos(\phi/2) + i \sin(\phi/2) \cos(2\theta) & i \sin(\phi/2) \sin(2\theta) \\ i \sin(\phi/2) \sin(2\theta) & \cos(\phi/2) - i \sin(\phi/2) \cos(2\theta) \end{bmatrix}, \quad (\text{S48})$$

where  $\theta$  is the angle between the fast axis of the wave plate and p polarization (the direction of LO), and  $\phi$  is the retardance of the wave-plate ( $\phi = \pi$  or  $\phi = \pi/2$  for an ideal  $\lambda/2$  or  $\lambda/4$  wave-plate, respectively). We fix the  $\lambda/4$  wave plate at  $\theta = 45^\circ$  and put the  $\lambda/2$  wave plate at a variable angle  $\theta_v$ , resulting in the output Jones vector

$$J_{out} = M_{\lambda/2}(\theta_v) M_{\lambda/4}(45^\circ) J_{in} = \begin{bmatrix} J_1 \\ J_2 \end{bmatrix} \quad (\text{S49})$$

with

$$\begin{aligned} J_1 &= \frac{1}{\sqrt{2}} \left[ i E_{LO} e^{i(2\theta_v - \phi_{LO})} - E_{SP} e^{-i(2\theta_v + \phi_{SP})} \right] \\ J_2 &= \frac{1}{\sqrt{2}} \left[ E_{LO} e^{i(2\theta_v - \phi_{LO})} - i E_{SP} e^{-i(2\theta_v + \phi_{SP})} \right]. \end{aligned} \quad (\text{S50})$$

Therefore, the interference between the two polarization modes observed at the two diodes of the HD after the second PBS is:

$$I_{HD} = |J_1|^2 - |J_2|^2 = 2E_{SP}E_{LO} \sin(4\theta_v - \phi_d), \quad (\text{S51})$$

where  $\phi_d = \phi_{SP} - \phi_{LO}$  is the initial phase difference between OPO output and LO mode before being overlapped at the first PBS. The result show that if we rotate the  $\lambda/2$  wave plate by an angle of  $1^\circ$ , the phase between LO and OPO output will change  $4^\circ$ . The form of Eq. (S51) also shows the visibility of the HD is not affected by the polarization transformation since it doesn't have any constant term. However, if the wave plates or PBS are not perfect, which means that the wave plates have either more or less retardance or that the PBS has a finite extinction ratio between s and p polarization, a similar calculation shows the rotation of  $\lambda/2$  wave plate by  $1^\circ$  will result in a phase shift slightly deviating from  $4^\circ$ , and that the visibility of the interference at HD can be reduced. We experimentally measure these imperfections as shown in the following subsection.

### B. Phase calibration

During the experiment we lock  $\phi_d$  to be either  $0^\circ$  or  $90^\circ$  with  $HD_L$ , and use the rotation of the  $\lambda/2$  wave plate before each HD to control the phase of each mode. In order to account for potential imperfections in our experiment, we first measured the visibility reduction from imperfect polarization components. We find a worst-case reduction of the HD visibility from 98.5% to 95.2%. We also perform a phase calibration by scanning the phase between LO and SP carrier with a ramp at 27 Hz while the interference fringe measured from  $V_{dc}$  of  $HD_L$  and  $HD_{1,2,3,4}$  is recorded. The phase between LO and signal in each path is inferred from sine curve fitting. We calibrate the phase with 40 repeated measurements at each  $\lambda/2$  wave plate position, and the result is shown in Fig. S8. The SQ (blue dots) shows the result when we lock  $\phi_i = 0^\circ$  and the HDs measure the squeezed quadrature, and the ASQ (red dots) shows the result when we lock  $\phi_i = 90^\circ$ . For both SQ and ASQ, we rotate the  $\lambda/2$  wave-plate position in each channel by an actuator in the wave-plate mount, allowing us to faithfully use the calibration result in the experiment.

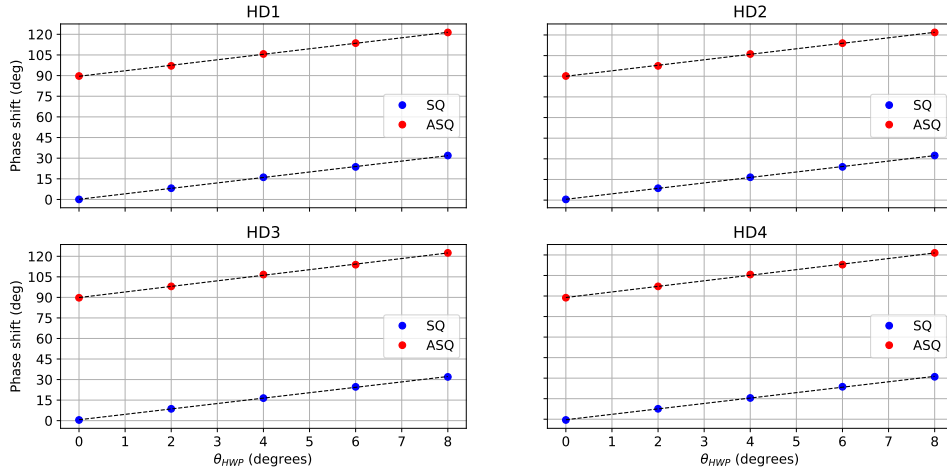


FIG. S8. Phase calibration result for each HD. The black dashed line is the linear fitting of the calibration.

TABLE I. The phase calibration result

Squeezing							
k1	-3.96	k2	-3.97	k3	-3.95	k4	-3.96
b1	-0.13	b2	-0.59	b3	-0.64	b4	0.37
Anti-squeezing							
k1	-3.99	k2	-3.99	k3	-4.06	k4	-4.06
b1	-89.50	b2	-89.97	b3	-89.87	b4	-88.90

From the calibration results, we see that the phase is linear within the whole range of the actuator ( $8^\circ$ ) on the wave plate mounts. The result of the linear fitting to HD channel  $j = 1$  to 4 with the equation

$$\phi_j = k_j \theta_v + b_j \quad (\text{S52})$$

is summarized in Table I. With these fitted parameters, we can control both the phase in each channel  $\phi_j$  or the averaged phase  $\phi_{\text{avg}}$  accurately. Particularly, if we lock  $\phi_i$  to  $0^\circ$ , we can change the  $\phi_{\text{avg}}$  by a slope of  $3.96^\circ \pm 0.02^\circ$ ; if we lock  $\phi_i$  to  $90^\circ$ , can change the  $\phi_{\text{avg}}$  by a slope of  $4.02^\circ \pm 0.02^\circ$ .

## V. DATA ANALYSIS

In this section we introduce the details of our data analysis procedure, which includes measuring the sensitivity by fitting and counting how many photons in average is used in the SP.

As the estimator of  $\phi_{\text{avg}}$ ,  $\hat{P}_{\text{avg}}$  is experimentally estimated from the PSD of the averaged output of the four HDs in each mode. Fig. S9 shows the PSD results measured for different  $\phi_{\text{avg}}$ . Each PSD is obtained from the FFT of an average of 2000 oscilloscope traces. The spectrum peak at 3 MHz  $S_{pk}$  gives the value of

$$S_{pk} = 2V_{sn}^2 \cdot \langle \hat{P}_{\text{avg}}^2 \rangle = 2V_{sn}^2 \cdot (\langle \Delta \hat{P}_{\text{avg}}^2 \rangle + \langle \hat{P}_{\text{avg}} \rangle^2), \quad (\text{S53})$$

where  $V_{sn}$  is the 4-mode shot noise limit (SNL) voltage from HDs decided by LO power, electronic gain and the digital filtering. The constant 2 in Eq. (S53) comes from the commutation relationship we choose  $[\hat{X}, \hat{P}] = i$ . We start our data analysis by separating the peak into two voltage parts

$$S_{pk} = V_s^2 + V_n^2, \quad (\text{S54})$$

where  $V_s = \sqrt{2}V_{sn}|\langle \hat{P}_{\text{avg}} \rangle|$  is the signal part induced by the coherent photons of the side band, and  $V_n = \sqrt{2}V_{sn}\sqrt{\langle \Delta \hat{P}_{\text{avg}}^2 \rangle}$  is the part induced by the fluctuation of the light. Except at the 3 MHz peak, the spectra in Fig. S9 vary slowly with frequency. This enables us to extract  $V_n$  from the adjacent frequencies of the 3 MHz peak. The procedure of  $V_n$  estimation is illustrated with the anti-squeezing quadrature (ASQ,  $\phi_{\text{avg}} = -89.5 \pm 0.8^\circ$ ) PSD in Fig. S9 as an example. We first do a linear fit with the frequency range indicated by the red dots, which is a slightly away from 3 MHz. This fitting gives the black dashed line labeled as "Fitting for ASQ".  $V_n$  is then inferred by the square root value of the fitted line at 3 MHz. Since our side band line width is obviously smaller than the 5 kHz resolution of the FFT, only one peak point is observed in the PSDs in Fig. S9. Therefore,  $V_s$  can simply be calculated by the difference between the blue dot at 3 MHz and the fitting result.

In our experiment we always introduce equal positive phase shift in all channels. In this case we know that  $\langle \hat{P}_{\text{avg}} \rangle > 0$ , and  $V_s$  and  $V_n$  relate to the averaged phase  $\phi_{\text{avg}}$  by

$$\begin{aligned} V_s(\phi_{\text{avg}}) &= \sqrt{2}V_{sn}\langle \hat{P}_{\text{avg}} \rangle = \frac{2}{\sqrt{M}}V_{sn} \cdot \alpha_e |\sin(\phi_{\text{avg}} + \theta_1)| \\ V_n(\phi_{\text{avg}}) &= \sqrt{2}V_{sn}\sqrt{\langle \Delta \hat{P}_{\text{avg}}^2 \rangle} = V_{sn} \cdot \sqrt{v_{sq}^2 \cos^2(\phi_{\text{avg}} + \theta_2) + v_{asq}^2 \sin^2(\phi_{\text{avg}} + \theta_2)}. \end{aligned} \quad (\text{S55})$$

Here  $\alpha$  is the real coherent amplitude from modulation,  $M$  is the mode number,  $\theta_1$  and  $\theta_2$  are parameters indicating the imperfections of the experimental setup (ideally they should be 0), where  $\theta_1$  parametrizes the residual amplitude modulation of the phase modulating EOM and  $\theta_2$  parametrizes the phase locking offset of the squeezing measurement.  $v_{sq}^2 = \eta e^{-2r_e} + (1 - \eta)$  and  $v_{asq}^2 = \eta e^{2r_e} + (1 - \eta)$  are squeezing and anti-squeezing degrees in SNL units. Note that the form of Eq. (S55) rely on two assumptions: First, we assume that the modulation signal on the EOM is perfectly coherent so  $V_s(\phi_{\text{avg}})$  doesn't have an offset term. This assumption is consolidated by the fact that we drive the EOM with a sine wave generated from a function generator with phase noise less than -65 dBc. Second, we ignore the phase fluctuations of the phase locking. This assumption is consolidated by the high ( $\sim 32$  dB) signal-to-noise ratio of the locking detector  $\text{HD}_L$ , though this signal-to-noise ratio is not a direct measurement of the phase fluctuation.

### A. Sensitivity fitting

With  $V_s$  and  $V_n$  extracted for a range of  $\phi_{\text{avg}}$  settings, we can estimate the sensitivity. By comparing the definition of  $\sigma$  in Eq. (S4) with Eq. (S55), the sensitivity to a small phase shift at a given  $\phi_{\text{avg}}$  offset is

$$\sigma = V_n(\phi_{\text{avg}})/V_s'(\phi_{\text{avg}}), \quad (\text{S56})$$

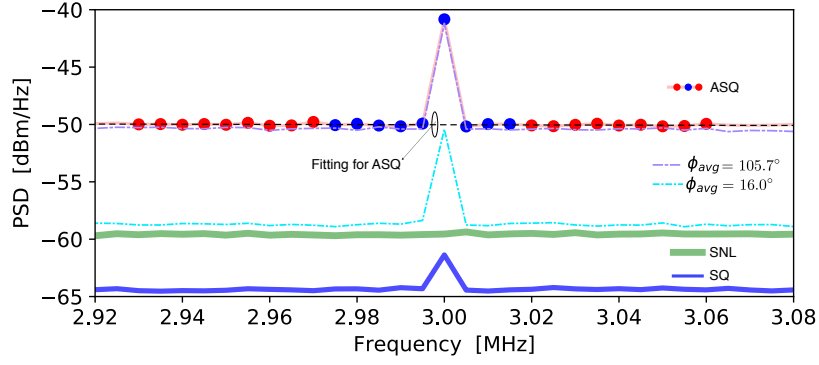


FIG. S9. PSDs of averaged HD output voltage with 3 MHz phase modulation on at different  $\phi_{\text{avg}}$ . SNL: shot-noise limit; SQ,  $\phi_{\text{avg}} = 0.2 \pm 0.8^\circ$ ; ASQ,  $\phi_{\text{avg}} = 89.5 \pm 0.8^\circ$ . We estimate  $V_s$  and  $V_n$  from these PSDs.

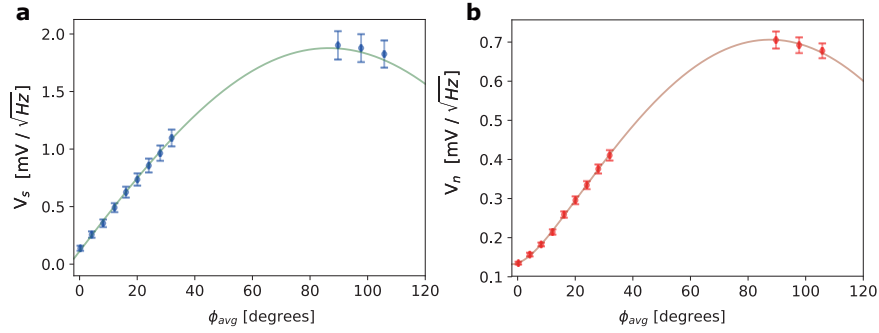


FIG. S10. (a) and (b): Fitting from measured  $V_s$  and  $V_n$  in different  $\phi_{\text{avg}}$ . With the fitting result,  $\sigma$  is estimated by using Eq. (S57).

where  $V'_s = \partial V_s / \partial \phi_{\text{avg}}$  is the partial derivative of  $V_s$  with respect to  $\phi_{\text{avg}}$  and the  $\sigma$  estimation is independent of SNL measurement since dividing  $V_n$  with  $V'_s$  can cancel  $V_{sn}$  out.

In the experiment we give an identical local phase shift to all 4 modes so that  $\phi_j = \phi_{\text{avg}}$  for all  $j = 1$  to 4, and change the value of  $\phi_{\text{avg}}$  around both the squeezing  $\phi_{\text{avg}} = 0$  and the anti-squeezing  $|\phi_{\text{avg}}| = 90^\circ$ . The  $\phi_{\text{avg}}$  we choose to induce as well as the fitting to Eq. (S55) with measured  $V_s$  and  $V_n$  from Figure S9 is shown in Figure S10. In the  $V_s(\phi_{\text{avg}})$  fitting, the parameters to fit are the slope  $k = \sqrt{\frac{2}{M}} V_{sn} \alpha_e$  and  $\theta_1$ . In the  $V_n$  fitting, the squeezing noise voltage scaled by SNL,  $k_{sq} = V_{sn} \cdot v_{sq}$ , the anti-squeezing noise voltage scaled by SNL,  $k_{asq} = V_{sn} \cdot v_{asq}$ , and  $\theta_2$  are fitting parameters. With the fitting result, we estimate the small angle sensitivity of our system  $\sigma_{\text{min}}$  by

$$\sigma_{\text{min}} = \frac{V_n(\phi_{\text{avg}} = 0)}{V'_s(\phi_{\text{avg}} = 0)}. \quad (\text{S57})$$

We do fitting for 5 different pump power of OPO and find the fitted values of  $\theta_1$  and  $\theta_2$  are  $3.4^\circ \pm 0.2^\circ$  and  $1.6^\circ \pm 0.6^\circ$ , respectively. These values are reasonably small, and in principle could be further reduced by better locking and phase modulation techniques. For the most sensitive case (maximum squeezing rate) in our result, the fitted  $\theta_1$  and  $\theta_2$  indicate  $\sigma_{\text{min}}$  could have been further improved by  $\sim 0.2\%$  and  $\sim 0.9\%$ , respectively. The  $\sigma_{\text{min}}$  extracted in Eq. (S57) is shown in our experiment results for the entangled approach in main text Fig 3 as  $\sigma_e$ .

A similar analysis method is used for the separable approach, but the PSDs used in the separable approach are from only one HD instead of averaged HD outputs. By removing the BSN, our setup gives the separable approach of  $M = 1$ . To compare with the entangled approach of  $M = 4$ , we rescale our result with  $1/\sqrt{M}$  as a result of classical averaging. The scaled sensitivity is quoted as our experiment result for the separable approach in main text Fig 3 as  $\sigma_s$ .



## B. Resource counting

In this section, we show how to experimentally measure the average photon number per mode that we use in the phase sensing.

For the entangled approach, we estimate  $MN_e = MN_{e,coh} + MN_{e,sqz}$  by comparing the joint measurement PSDs for squeezing and anti-squeezing quadrature to that for SNL, where  $M = 4$  is the mode number. With the notation defined above, the average number of squeezed photons for all modes in the entangled approach are obtained by comparing  $V_n$  to  $V_{sn}$  with

$$M \cdot N_{e,sqz} = \frac{1}{2} \left( \langle \Delta \hat{P}_{avg}^2 \rangle + \langle \Delta \hat{X}_{avg}^2 \rangle - 1 \right) = \frac{1}{4} \left[ \frac{V_n^2(\phi_{avg} = 0^\circ)}{V_{sn}^2} + \frac{V_n^2(\phi_{avg} = 90^\circ)}{V_{sn}^2} - 2 \right], \quad (S58)$$

Similarly, the average number of coherent photons are obtained by comparing  $V_s$  to  $V_{sn}$  with

$$M \cdot N_{e,coh} = \eta \alpha_e^2 = \frac{V_s^2(\phi_{avg} = 90^\circ)}{4V_{sn}^2}. \quad (S59)$$

With Eq. (S58) and (S59),  $N_e = N_{e,coh} + N_{e,sqz}$  gives the  $N$  values in main text Fig 3 for the entangled approach  $\sigma_e$ .

For the separable approach, we use a very similar technique. However, the PSD is from a single HD instead of joint measurement. Explicitly, the photon number per mode for the separable approach is  $N_s = N_{s,coh} + N_{s,sqz}$ , with

$$N_{s,sqz} = \frac{1}{2} \left( \langle \Delta \hat{p}_j^2 \rangle + \langle \Delta \hat{x}_j^2 \rangle - 1 \right) = \frac{1}{4} \left[ \frac{V_n^2(\phi = 0^\circ)}{V_{sn'}^2} + \frac{V_n^2(\phi = 90^\circ)}{V_{sn'}^2} - 2 \right] \quad (S60)$$

and

$$N_{s,coh} = \frac{V_s^2(\phi = 90^\circ)}{4V_{sn'}^2}, \quad (S61)$$

where  $\phi$  is the phase shift of the single mode, and we use  $V_{sn'}$  to denote the 1-mode SNL, which is about 1/4 of the 4-mode SNL  $V_{sn}$  used in the entangled approach. The photon number per mode  $N_s = N_{s,coh} + N_{s,sqz}$  gives the  $N$  values in main text Fig 3 for the separable approach  $\sigma_s$ .

- 
- [S1] T. J. Proctor, P. A. Knott, and J. A. Dunningham, Phys. Rev. Lett. **120**, 080501 (2018).
  - [S2] A. A. Berni, T. Gehring, B. M. Nielsen, V. Händchen, M. G. Paris, and U. L. Andersen, Nature Photonics **9**, 577 (2015).
  - [S3] C. W. Helstrom, Academic Press, New York (1976).
  - [S4] A. S. Holevo, North-Holland, Amsterdam (1982).
  - [S5] M. Gessner, L. Pezzè, and A. Smerzi, Phys. Rev. Lett. **121**, 130503 (2018).
  - [S6] M. Aspachs, J. Calsamiglia, R. Muñoz Tapia, and E. Bagan, Phys. Rev. A **79**, 033834 (2009).
  - [S7] O. Pinel, P. Jian, N. Treps, C. Fabre, and D. Braun, Phys. Rev. A **88**, 040102 (2013).
  - [S8] A. Monras and M. G. A. Paris, Phys. Rev. Lett. **98**, 160401 (2007).
  - [S9] C. Oh, C. Lee, C. Rockstuhl, H. Jeong, J. Kim, H. Nha, and S.-Y. Lee, npj Quantum Information **5**, 10 (2019).
  - [S10] L. Neuhaus, R. Metzдорff, S. Chua, T. Jacqmin, T. Briant, A. Heidmann, P.-F. Cohadon, and S. Deléglise, in *European Quantum Electronics Conference* (Optical Society of America, 2017) p. EA\_P.8.
  - [S11] P. Grangier, R. E. Slusher, B. Yurke, and A. LaPorta, Phys. Rev. Lett. **59**, 2153 (1987).
  - [S12] E. Polzik, J. Carri, and H. Kimble, Applied Physics B **55**, 279 (1992).
  - [S13] G. Vidal and R. F. Werner, Physical Review A **65**, 032314 (2002).
  - [S14] E. Collett, SPIE Press, Bellingham, WA (2005).